OPEN ACCESS



The MASSIVE Survey. XX. A Triaxial Stellar Dynamical Measurement of the Supermassive Black Hole Mass and Intrinsic Galaxy Shape of Giant Radio Galaxy NGC 315

Jacob Pilawa ¹ ¹ ¹, Emily R. Liepold ¹ ¹, Chung-Pei Ma ^{1,2} ¹, Jonelle L. Walsh ³ ¹, and Jenny E. Greene ⁴ ¹ Department of Astronomy, University of California, Berkeley, CA 94720, USA; jacobpilawa@berkeley.edu ² Department of Physics, University of California, Berkeley, CA 94720, USA

³ George P. and Cynthia Woods Mitchell Institute for Fundamental Physics and Astronomy, and Department of Physics and Astronomy, Texas A&M University, College Station, TX 77843, USA

⁴ Department of Astrophysical Sciences, Princeton University, Princeton, NJ 08544, USA Received 2025 March 31; revised 2025 July 7; accepted 2025 July 8; published 2025 August 7

Abstract

We present a new dynamical measurement of the supermassive black hole mass and intrinsic shape of the stellar halo of the massive radio galaxy NGC 315 as part of the MASSIVE survey. High signal-to-noise ratio spectra from integral-field spectrographs at the Gemini and McDonald Observatories provide stellar kinematic measurements in 304 spatial bins from the central ~0."3 out to 30". Using ~2300 kinematic constraints, we perform triaxial stellar orbit modeling with the TriOS code and search over ~15,000 galaxy models with a Bayesian scheme to simultaneously measure six mass and intrinsic shape parameters. NGC 315 is triaxial and highly prolate, with middle-to-long and short-to-long axis ratios of p = 0.854 and q = 0.833, and a triaxiality parameter of T = 0.89. The black hole mass inferred from our stellar kinematics is $M_{\rm BH} = (3.0 \pm 0.3) \times 10^9~M_{\odot}$, which is higher than $M_{\rm BH} = (1.96^{+0.30}_{-0.13}) \times 10^9 M_{\odot}$ inferred from CO kinematics (scaled to our distance). When the seven galaxies with $M_{\rm BH}$ measurements from both stellar and CO kinematics are compared, we find an intrinsic scatter of 0.28 dex in $M_{\rm BH}$ from the two tracers and do not detect statistically significant biases between the two methods in the current data. The implied black hole shadow size ($\approx 4.7~\mu as$) and the relatively high millimeter flux of NGC 315 makes this galaxy a prime candidate for future horizon-size imaging studies.

Unified Astronomy Thesaurus concepts: Galaxies (573); Supermassive black holes (1663); Stellar dynamics (1596); Galaxy evolution (594); Dark matter (353); Elliptical galaxies (456)

1. Introduction

The MASSIVE survey is a volume-limited, photometric, and spectroscopic survey of the ~100 most massive early-type galaxies (with stellar mass $M_* \gtrsim 10^{11.5} M_{\odot}$) in the local Universe (C.-P. Ma et al. 2014). A key scientific goal of the survey is to dynamically measure the masses of a sample of supermassive black holes (SMBHs) within the targeted volume (to a distance of ~ 100 Mpc above decl. $\delta = -6^{\circ}$) with spatially resolved stellar and gas (when present) kinematics. To date, 14 MASSIVE galaxies have published dynamical SMBH mass $(M_{\rm BH})$ measurements as compiled in Table 1 of E. R. Liepold & C.-P. Ma (2024). Among them, only M87 has $M_{\rm BH}$ determined from the motion of more than one type of dynamical tracer. For the rest, nine galaxies⁵ have $M_{\rm BH}$ determined from stellar kinematics using the Schwarzschild orbit modeling method, three galaxies 6 have $M_{\rm BH}$ inferred from CO kinematics, and one galaxy⁷ is studied with ionized gas.

In this work, we report a new mass measurement of the SMBH in NGC 315 using stellar kinematics from MASSIVE survey observations and the triaxial orbit modeling method.

Original content from this work may be used under the terms of the Creative Commons Attribution 4.0 licence. Any further distribution of this work must maintain attribution to the author(s) and the title of the work, journal citation and DOI.

NGC 315 has a prior $M_{\rm BH}$ determination based on CO kinematics from Atacama Large Millimeter/submillimeter Array (ALMA) observations (B. D. Boizelle et al. 2021). NGC 315 is therefore only the second galaxy in the MASSIVE survey for which a direct comparison of $M_{\rm BH}$ from different dynamical tracers can be made. Beyond MASSIVE, six other galaxies have $M_{\rm BH}$ inferred from both ALMA CO kinematics and stellar kinematics, enabling us to assess the consistency between the two methods (see Section 4). NGC 315 is also only the fifth MASSIVE galaxy for which the triaxial stellar-orbit modeling is used to determine its $M_{\rm BH}$ (others assumed axisymmetry), and is the first MASSIVE galaxy with $M_{\rm BH}$ determined from both CO and triaxial stellar-based methods.

NGC 315 is the brightest member of a galaxy group identified in the Two Micron All Sky Survey group catalog (A. C. Crook et al. 2007). The high-density contrast and low-density contrast versions of the catalog list 6 and 97 member galaxies, respectively. The halo virial mass is estimated to be $3.5 \times 10^{13} M_{\odot}$ based on member galaxy velocities. NGC 315 has strong nuclear radio emission (B. L. Fanaroff & J. M. Riley 1974) and a prominent jet extending $\gtrsim 100''$ at a position angle (PA) of $\sim -50^{\circ}$ (R. A. Laing et al. 2006; L. Ricci et al. 2022). NGC 315 is one of seven MASSIVE survey targets with evidence for an X-ray point source in the nuclear region in the 4–7 keV band. The mean temperature and luminosity of the X-ray hot gas are estimated to be $T_{\rm X} = 0.57$ keV and $L_{\rm X} = 3.8 \times 10^{41}$ erg s⁻¹ (A. D. Goulding et al. 2016).

Typical of MASSIVE galaxies, NGC 315 is a slow rotator with a velocity amplitude of $\sim 30~\rm km~s^{-1}$ and a spin parameter of $\lambda = 0.063$ (M. Veale et al. 2017b; I. Ene et al. 2019). The

⁵ NGC 708, NGC 1453, NGC 1600, NGC 2693, NGC 3842, NGC 4472, NGC 4649, NGC 4889, NGC 7619.

⁶ NGC 315, NGC 997, NGC 1684.

⁷ NGC 7052.

PA of the kinematic axis (measured E of N to the receding portion) is determined to be $PA_{kin}=222^{\circ}\pm7^{\circ}$ over the $107^{''}\times107^{''}$ field of view (FOV) of the Mitchell integral-field spectrograph (IFS, I. Ene et al. 2018), and $PA_{kin}=218^{\circ}\pm13^{\circ}$ in the central $5^{''}\times7^{''}$ region from Gemini IFS data (I. Ene et al. 2020). The $\sim90^{\circ}$ offset between the kinematic axis and the jet indicates the projection of the angular momentum vector of the stars onto the sky is at the same PA as the jet. HST photometry shows boxy isophotes and nearly constant ellipticity and photometric PA between a radius of $1^{''}$ and $100^{''}$ with luminosity-weighted values of $\epsilon=0.27$ and $PA_{phot}=44^{\circ}.3\pm0^{\circ}.2$ (Figure 1.2 of C. F. Goullaud et al. 2018). The kinematic misalignment angle is consistent with 0: $\Psi=6^{\circ}.3\pm13^{\circ}.3$ (I. Ene et al. 2020).

In Section 2, we discuss the IFS data from Gemini and McDonald Observatories and the stellar velocity moment measurements reported in M. Veale et al. (2017a, 2017b, 2018) and I. Ene et al. (2018, 2019, 2020). The HST observations of NGC 315 (C. F. Goullaud et al. 2018) and surface brightness profile determination (B. D. Boizelle et al. 2021) are also summarized. In Section 3, we summarize the triaxial orbit modeling code TriOS (M. E. Quenneville et al. 2021, 2022) and the parameter search strategy used to select galaxy models, followed by a discussion of the mass and shape parameters and stellar orbital structure that best match the observations. Section 4 discusses systematic uncertainties and compares $M_{\rm BH}$ determined from stellar versus CO kinematics.

Throughout this work, we assume a luminosity distance for NGC 315 of $D_L = 68.1 \pm 2.5$ Mpc from the MASSIVE-HST project using the surface brightness fluctuation technique (C. F. Goullaud et al. 2018; J. P. Blakeslee et al. 2021; J. B. Jensen et al. 2021). At NGC 315's redshift of z = 0.0165, the corresponding angular diameter distance is $D_A = 65.9 \pm 2.4$ Mpc, and 1" is 320 pc. When comparing with B. D. Boizelle et al. (2021), we adjust their reported values from their assumed $D_A = 70$ Mpc to our distance.

2. Observations

2.1. Photometry

NGC 315 has a prominent circumnuclear dust disk in the central $\sim 1^{''}$ region. B. D. Boizelle et al. (2021) produce three multi-Gaussian expansion (MGE) models (A, B2, and B3) of the mosaiced image, applying a differing amount of extinction correction to the nuclear region. The central Gaussian component in B2 and B3 has a width of $\sigma'=0\rlap.{''}178$ and $\sigma'=0\rlap.{''}119$, respectively, comparable to the point-spread function (PSF) ($\sim\!0\rlap.{''}15$). As discussed in E. R. Liepold et al. (2025), the width of the central component is poorly constrained when it is comparable or below the scale of the PSF. The MGE routine sometimes assigns a central component with $\sigma'\lesssim\sigma'_{\rm PSF}$ that does not improve the fit in a meaningful

way but results in an exceptionally large central 3D density after deprojection (recall $\nu \propto \Sigma/\sigma'$ where Σ is the central surface brightness). Accordingly, the B2 and B3 MGEs have a "bump" in their luminosity densities in the central region, as shown in the Appendix. Additional examples of this artifact can be found in J. R. Davidson et al. (2024). E. R. Liepold et al. (2025) circumvented this problem by imposing a lower limit on σ' during the MGE fitting. Here, we adopt MGE model A, which has $\sigma' = 0.\%580$ for the central component and a smooth 3D deprojected density profile without this stellar excess. In Section 4.1, we describe results from tests using model B3, the case with the most extreme central luminosity density.

2.2. Integral-field Spectroscopy

2.2.1. Central Stellar Kinematics

We observed the central $5'' \times 7''$ of NGC 315 using the two-slit IFS mode of Gemini Multi-Object Spectrograph (GMOS) on the Gemini North Telescope with 1000 hexagonal lenslets (each with a projected diameter of 0.22). Ten science exposures of 1200 s each were obtained, totaling 3.3 hr of on-source and simultaneous observations of a $5'' \times 3''.5$ region of sky offset by $\sim 1'$ from the galaxy. The R400-G5305 grating with the CaT filter was used to cover the wavelength range 7800–9330 Å. The median spectral resolution (determined from arc lamp lines for each lenslet) was 2.5 Å FWHM. Details of the data processing procedure are described in MASSIVE Paper XIII (I. Ene et al. 2019).

We coadd the spectra from a group of adjacent GMOS lenslets to achieve a threshold signal-to-noise ratio (S/N) of 125. This binning procedure results in 248 high-quality spectra covering the central region of NGC 315. One difference in this step from I. Ene et al. (2019) is that a symmetric binning scheme over the four quadrants of the galaxy was used in that work, while here we perform the binning over the entire GMOS FOV without this assumption. This difference only introduces minor adjustments in how the GMOS lenslets are grouped spatially; the stellar kinematics are measured for each bin without any symmetry assumption in both analyses.

From each spectrum, we measure the line-of-sight velocity distribution (LOSVD) from the Ca II triplet (CaT) absorption features over a rest wavelength range of 8420–8770 Å using the penalized pixel-fitting method (M. Cappellari 2017). The LOSVD is represented as a Gauss–Hermite series of order n=8. We use 15 stellar templates from the MILES CaT Library that covers a wavelength range of 8437–9020 Å with a spectral resolution of 1.5 Å FWHM (A. J. Cenarro et al. 2001). This set of stars is taken from Table 2 of A. J. Barth et al. (2002), but we find consistent stellar kinematics when the full library of 706 stars is used. A multiplicative polynomial of degree three is used to model the stellar continuum in each spectrum.

Four representative spectra at increasing radii are plotted in Figure 1. The template spectrum broadened by the best-fit LOSVD (blue curve) provides an excellent fit to each observed spectrum (black curve) with a typical residual (red points) of $\sim 0.5\%$. In addition to the bright sky lines, the wavelength range $\gtrsim 8750$ Å is also masked due to the presence of a gap in the CCD chip. The resulting maps of the eight Gauss–Hermite moments of the LOSVDs for the 248 GMOS spatial bins are shown in Figure 2. The corresponding radial profiles of the

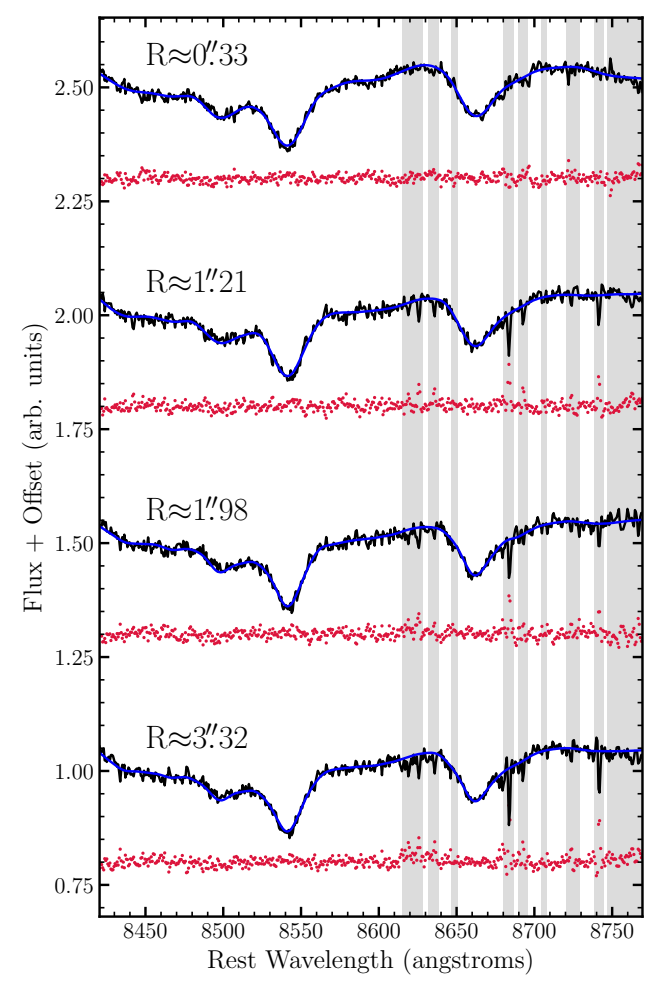


Figure 1. Four representative Gemini GMOS spectra (black) of NGC 315 for spatial bins located at increasing distance from the nucleus. The stellar template broadened by the best-fit LOSVD is overlaid (blue) on each spectrum. The fitting residuals (red points) are offset by constants for clarity. The typical residual is $\sim 0.5\%$. The gray shaded regions are excluded from the fit to account for improperly subtracted sky lines and detector gap.

eight moments are displayed as blue bars in Figure 3. The errors on the moments are determined via the Monte Carlo method described in Section 4 of I. Ene et al. (2019). These figures show a velocity profile with a low amplitude rotational velocity $|V| \sim 20 \, \mathrm{km \, s^{-1}}$, and a velocity dispersion profile that rises from $\sigma \sim 320 \, \mathrm{km \, s^{-1}}$ at $R \sim 2''$ inward to $\sigma \sim 350 \, \mathrm{km \, s^{-1}}$ at $R \sim 0''.3$.

2.2.2. Wide-field Stellar Kinematics

We observed NGC 315 with the Mitchell IFS at the McDonald Observatory as part of the MASSIVE Survey. Details of the observation, data reduction, and kinematic measurements are described in M. Veale et al. (2017a, 2017b, 2018). The observations consisted of three dither positions, during which we interleaved two 20 minutes science frames with one 10 minutes sky frame, resulting in 2 hr on-source. Each frame spans a $107^{"} \times 107^{"}$ FOV with 246 fibers, covering a wavelength range of 3650-5850 Å that includes the Ca HK region, the *G*-band region, $H\beta$, Mgb, and several Fe lines. The individual fibers in the central region of NGC 315 provide spectra with $S/N \gtrsim 50$. For the fainter part of the galaxy

covered by the outer fibers, the spectra are coadded to achieve $S/N \gtrsim 20. \label{eq:spectra}$

The LOSVD from each Mitchell spectrum is extracted in a similar way as GMOS described above. We opt to fit to n=6 Gauss–Hermite moments due to the lower S/N data here. The MILES library of 985 stellar spectra is used as templates (P. Sanchez-Blazquez et al. 2006; J. Falcón-Barroso et al. 2011). The kinematic moments for the 55 Mitchell bins are shown in Figure 3 in pink. The Mitchell data points connect smoothly to the GMOS points, showing excellent agreement between measurements obtained from different spectrographs, telescopes, and spectral regions. Six additional kinematic points at $R \sim 50^{\circ}$ are shown in Figure D1 of M. Veale et al. (2017b) but are excluded in the following analysis due to the low S/N of these outer spectra.

3. Results from Triaxial Orbit Modeling

3.1. The TriOS Code and Galaxy Models

We use the TriOS code (R. C. E. Van Den Bosch et al. 2008; M. E. Quenneville et al. 2021, 2022) to compute triaxial orbit models of NGC 315. This code integrates a large number of stellar orbits that span the allowed phase space and computes the LOSVDs for a wide range of galaxy model parameters. The galaxy is assumed to have three mass components: a central black hole of mass $M_{\rm BH}$, a stellar component with a mass-to-light ratio M^*/L , and a dark matter halo with a density profile $\rho(r) = \rho_0/[(r/r_s)^{\gamma}(1 + r/r_s)^{3-\gamma}]$, where r_s is a scale radius (J. F. Navarro et al. 1996). We set $\gamma = 0$ so that the profile has a finite central density ρ_0 and a flattened central density distribution similar to that of the stars. With our data, r_s and ρ_0 are often quite degenerate so we choose to parameterize the halo with a single parameter, M_{15} , defined to be the dark matter mass enclosed within 15 kpc with a fixed scale radius $r_s = 15$ kpc. A similar strategy was used in orbit modeling of other MASSIVE galaxies (e.g., E. R. Liepold et al. 2020; J. D. Pilawa et al. 2022; M. E. Quenneville et al. 2022).

We use three parameters to specify the triaxial shape of the stellar component: p=b/a is the intrinsic middle-to-long axis ratio, q=c/a is the intrinsic short-to-long axis ratio, and u is the apparent-to-intrinsic long axis ratio. These three shape parameters are related to the three angles θ , ϕ , and ψ that relate the intrinsic and projected coordinate systems of NGC 315; see Equations (4) and (8) of M. E. Quenneville et al. (2022). Here, θ and ϕ are polar angles in NGC 315's intrinsic coordinate system, and ψ specifies the remaining degree of freedom—a rotation of the galaxy around the line of sight.

In total, each galaxy model has six free parameters— $M_{\rm BH}$, M^*/L , M_{15} , and three shape parameters—to be constrained by the kinematic and photometric data. For each model, we use the same procedures for phase space sampling and orbit integrations as in our earlier work (e.g., Section 4.1 of E. R. Liepold et al. 2023). We integrate the trajectories of stars to build a library of 437,400 stellar orbits. A dithering factor of $N_{\rm dither} = 3$ is used, where the properties of $N_{\rm dither}^3 = 27$ orbits with similar initial conditions are averaged, effectively giving them a single shared orbital weight. We determine the resulting 16,200 independent orbital weights using the kinematic measurements with non-negative least squares (C. L. Lawson & R. J. Hanson 1995), under the additional constraint that both the projected mass within each aperture and the 3D mass distribution in coarse bins are consistent

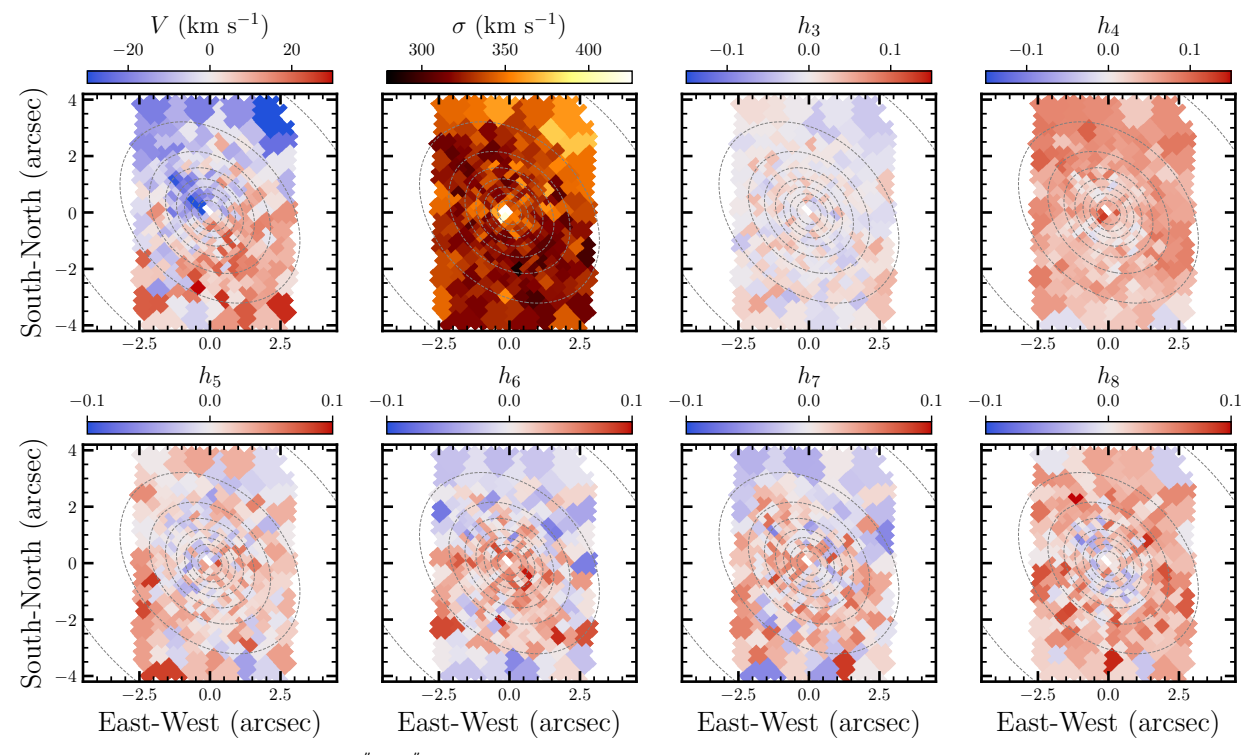


Figure 2. Stellar kinematic maps of the central $5'' \times 7''$ region of NGC 315 from Gemini GMOS observations. Spectra from individual lenslets are coadded to achieve a single spectrum with $S/N \gtrsim 125$ for each of the 245 spatial bins. The two upper-left panels show the line-of-sight velocities V and velocity dispersions σ , with the higher-order Gauss-Hermite moments h_3 to h_8 shown in the other panels. Surface brightness contours are plotted as dotted gray lines.

within 1% of the MGE. The GMOS and Mitchell PSFs are taken to be single, circularly symmetric Gaussians with FWHM of 0.38 and 1.2, respectively.

3.2. Best-fit Triaxial Model

We use the model selection scheme described in our recent work (e.g., J. D. Pilawa et al. 2022; E. R. Liepold et al. 2023, 2025) to determine the mass and shape parameters that best match the kinematic and photometric data of NGC 315. This scheme, in brief, involves generating candidate galaxy models with Latin hypercube sampling (M. D. McKay et al. 1979), approximating the resulting likelihood landscapes with Gaussian process regression, and sampling posteriors on our parameters via dynamic nested sampling (J. S. Speagle 2020). The relative likelihood for each model is computed from

$$-2\ln\mathcal{L}(\boldsymbol{\mu}) = \chi_{\text{kin}}^2(\boldsymbol{\mu}) = \sum_{j}^{N_{\text{bin}}} \sum_{i}^{N_{\text{GH}}} \frac{(h_{ij}(\boldsymbol{\mu}) - h_{ij,\text{data}})^2}{\Delta h_{ij,\text{data}}^2}, \quad (1)$$

where h_{ij} is the *i*th Gauss–Hermite moment of the stellar LOSVDs in the *j*th spatial bin, Δh_{ij} is the measurement uncertainty, and μ is the set of six parameters describing the galaxy's potential. To obtain 1D confidence intervals for each galaxy parameter, we take the marginalized distribution for each parameter to be the distribution of (weighted) sample points over the desired parameters, assuming uncertainties in the distribution function (e.g., orbital weights) are neglected.

About ~ 1750 galaxy models are used to obtain the final posteriors on the six parameters shown in Figure 4. An additional ~ 3000 models covering wider ranges of parameters are used in the initial exploration of the 6D likelihood surface,

and \sim 10,000 more models are used in various tests to ensure that the surface in the low χ^2 region is mapped out accurately.

A summary of the best-fit parameters for NGC 315 is listed in Table 1. The kinematic moments predicted by the model are compared with observed values in Figure 3. The total χ^2 is 1611.4 spread over 2314 kinematic constraints (eight moments for 248 GMOS bins and six moments for 55 Mitchell bins). A naive estimate of the reduced χ^2 would be 1611.4/(2314-6) = 0.698 assuming 6 degrees of freedom (dof). But we caution that dof is nontrivial to estimate for nonlinear problems such as here. In a study using simulated stellar kinematics that mimic data in the MASSIVE survey (J. Pilawa et al. 2024), we have investigated a "generalized" measure of dof in the form of a penalty term added to the likelihood measure (J. Ye 1998; M. Lipka & J. Thomas 2021) and found it to be \sim 200 instead of the canonical value of 6, thereby raising the reduced χ^2 by $\sim 40\%$ in that study. While a similar calculation would have to be performed to estimate this alternative dof measure for NGC 315, we expect the reduced χ^2 to be raised as well. Using this generalized measure to estimate the effective dof in the models also helps address a related concern that the conventional (unpenalized) likelihood method does not marginalize over the high dimensional space of possible orbital weights, leading to reliable $M_{\rm BH}$ but with "overly pessimistic error estimates" (J. Magorrian 2006). In J. Pilawa et al. (2024), we find that the parameter search and inference routines used in this paper and other work by our group (e.g., J. D. Pilawa et al. 2022; M. E. Quenneville et al. 2022; E. R. Liepold et al. 2023; J. Pilawa et al. 2024; E. R. Liepold et al. 2025) are able to reliably recover the mass and shape parameters associated with synthetic galaxy kinematic data without any additional penalty terms.

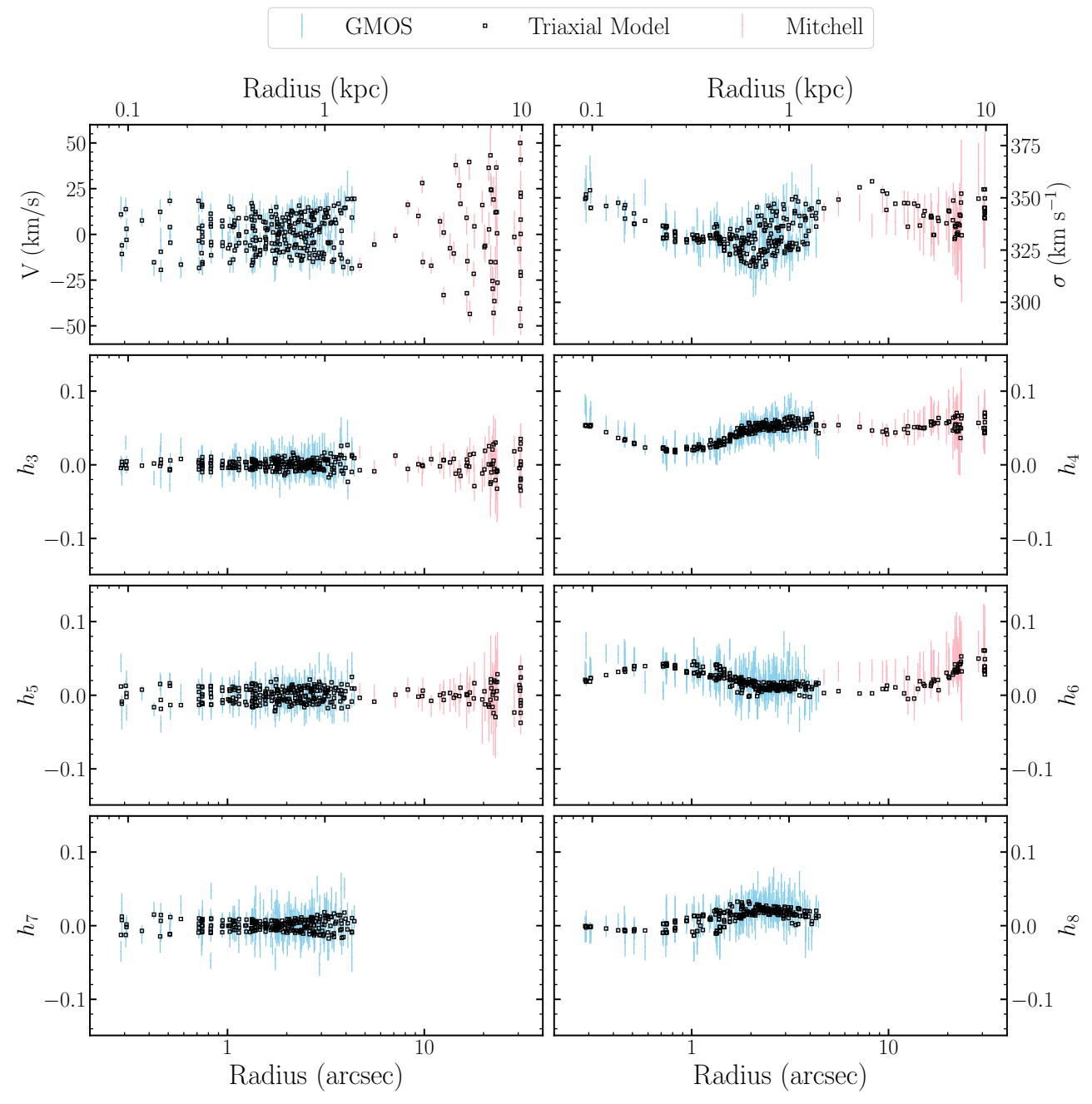


Figure 3. Radial profiles of the stellar kinematic moments for NGC 315 from Gemini GMOS (blue bars) and Mitchell (pink bars) data. Moments predicted by the best-fitting triaxial galaxy model (black squares) listed in Table 1 match the input data well.

A handful of the model predictions in Figure 3 lie outside the 68% uncertainties of the data points, e.g., the h_4 and h_6 GMOS moments within 0.16 are underpredicted (on average) by $\sim 1.05\sigma$ and $\sim 1.11\sigma$, respectively, and Mitchell's velocity dispersion and h_6 between 5 and 10 are over- and underpredicted by $\sim 1.1\sigma$ and $\sim 1.6\sigma$, respectively. These systematic local deviations occur in $\lesssim 2\%$ of the 2314 kinematic constraints. When excluding these deviant constraints from the χ^2 used for our parameter inference, we find an insignificant change in the inferred $M_{\rm BH}$.

3.2.1. Black Hole Mass, Stellar Mass, and Dark Matter Mass

To assess how NGC 315 and its SMBH fit in the population of local galaxies with dynamically inferred $M_{\rm BH}$,

we examine its location on the well-studied $M_{\rm BH}-\sigma$ and $M_{\rm BH}-M_{\rm bulge}$ relations. NGC 315's luminosity-weighted velocity dispersion within R_e is found to be σ_e = 341 km s⁻¹ based on the same Mitchell IFS data in this paper (M. Veale et al. 2017b). At this σ_e , the mean full-sample $M_{\rm BH}-\sigma$ relations of N. J. McConnell & C.-P. Ma (2013) and R. P. Saglia et al. (2016) predict $M_{\rm BH}$ = $4.2 \times 10^9 M_{\odot}$ and $3.3 \times 10^9 M_{\odot}$, respectively, 40% (0.15 dex) and 10% (0.04 dex) larger than our dynamically measured $M_{\rm BH}$. However, our $M_{\rm BH}$ is within the intrinsic scatter of both relations, 0.38 dex.

To place NGC 315 on the $M_{\rm BH}$ – $M_{\rm bulge}$ relation, we use the total stellar mass from our best-fitting triaxial model, $M_* = 1.5 \times 10^{12} M_{\odot}$. At this bulge mass, the mean full-sample

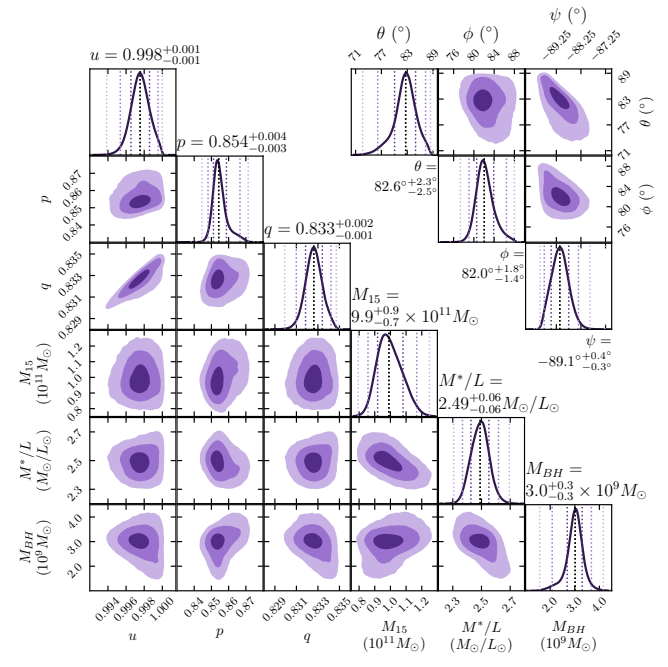


Figure 4. (Left) Posterior distributions of six parameters in triaxial orbit modeling of NGC 315: SMBH mass $M_{\rm BH}$, stellar mass-to-light ratio M^{\prime}/L , dark matter enclosed within 15 kpc M_{15} , and luminosity averaged axis ratios u, p, and q. The 68%, 95%, and 99.7% credible regions are represented by different shades of purple. The vertical lines in each 1D marginalized distribution indicate the median and the three corresponding confidence levels. (Upper right) Posterior distributions in viewing-angle space, where θ and ϕ are polar angles in the galaxy's frame, and ψ specifies a rotation of the galaxy around the line of sight (Section 2.2 of M. E. Quenneville et al. 2022).

Table 1
Galaxy Parameters of NGC 315 from Triaxial Orbit Modeling

Galaxy Property (Units)	Inferred Value
Black hole mass $M_{\rm BH}$ (10 ⁹ M_{\odot})	3.0 ± 0.3
$M^*/L \ (M_{\odot}/L_{\odot})$	2.49 ± 0.06
Total stellar mass $(10^{12} M_{\odot})$	1.5
DM mass within 15 kpc M_{15} ($10^{11} M_{\odot}$)	$9.9^{+0.9}_{-0.7}$
Triaxiality parameter T	0.89 ± 0.02
Shape parameter $T_{\rm maj}$	$0.019^{+0.008}_{-0.007}$
Shape parameter T_{\min}	$0.017^{+0.009}_{-0.013}$
Average middle-to-long axis ratio p	$0.854^{+0.004}_{-0.003}$
Average short-to-long axis ratio q	$0.833^{+0.002}_{-0.001}$
Average apparent-to-intrinsic long axis ratio u	0.998 ± 0.001
Line-of-sight direction $\theta(^{\circ})$, $\phi(^{\circ})$	$82.6^{+2.3}_{-2.5}, 82.0^{+1.8}_{-1.4}$
Rotation about line of sight $\psi(^{\circ})$	$-89.1^{+0.4}_{-0.3}$

Note. For each parameter, we marginalize over the other parameters and report the 68% credible regions. In orbit models, θ is the inclination angle in the oblate axisymmetric limit ($\psi=90^\circ$, or equivalently p=1), with $\theta=90^\circ$ being edge-on and $\theta=0^\circ$ being face-on.

relations of N. J. McConnell & C.-P. Ma (2013) and R. P. Saglia et al. (2016) predict $M_{\rm BH} = 5.3 \times 10^9 M_{\odot}$ and $4.4 \times 10^9 M_{\odot}$, respectively, 77% (0.25 dex) and 47% (0.17 dex) larger than our measured $M_{\rm BH}$. But again, our dynamical $M_{\rm BH}$ is within the intrinsic scatter of both $M_{\rm BH}$ – $M_{\rm bulge}$ relations, 0.34 dex.

In our preferred model, the black hole has a gravitational sphere of influence (SOI) of $r_{SOI} = 0.981 = 0.26$ kpc with the definition of $M^*(< r_{SOI}) = M_{BH}$, and $r_{SOI} = 1.99 = 1.99 = 1.99$ with the definition of $M^*(< r_{SOI}) = 2M_{BH}$.

Within the effective radius $R_e = 25.7$ (~ 8.3 kpc) of NGC 315 (M. E. Quenneville et al. 2024), the dark matter halo constitutes $\sim 47\%$ of the total mass of the galaxy. This value is broadly consistent with the rising dark matter fraction with increasing galaxy stellar mass reported for lower-mass early-type galaxies (e.g., Figure 10 of M. Cappellari et al. 2013; Figure 16 of G. Santucci et al. 2022), where the dark matter fraction (at $1 R_e$) reaches $\sim 40\%$ at the highest masses $(M^* \sim 5 \times 10^{11} M_{\odot})$ in their samples.

3.2.2. Intrinsic 3D Galaxy Shape

The preferred axis ratios of p=0.854 and q=0.833 yield a triaxiality parameter of $T=(1-p^2)/(1-q^2)=0.89\pm0.02$, where the limits of T=0 and 1 correspond to oblate axisymmetry and prolate axisymmetry, respectively. In comparison, five other massive elliptical galaxies for which we have performed triaxial orbit modeling thus far all have smaller T. Four of them are oblate $(T \le 0.5)$: $T=0.33\pm0.06$ for NGC 1453 (M. E. Quenneville et al. 2021), $T=0.39\pm0.04$ for NGC 2693 (J. D. Pilawa et al. 2022), $T=0.35\pm0.03$ for Holmberg 15A (E. R. Liepold et al. 2025), and $T=0.31\pm0.05$ for NGC 57 (J. Pilawa et al. 2025, in preparation). M87, on the other hand, is slightly prolate with $T=0.65\pm0.02$ (E. R. Liepold et al. 2023).

While the determinations of the intrinsic axis ratios p and q for individual galaxies require triaxial orbit modeling and detailed kinematic data, one can infer the distributions of p and q statistically from the observed isophotal shapes and kinematic versus photometric misalignment angles of an ensemble of galaxies. For slow-rotating galaxies in the MASSIVE survey, the mean values are found to be $\langle p \rangle = 0.88, \ \langle q \rangle = 0.65, \ \text{and} \ \langle T \rangle = 0.39$ (I. Ene et al. 2018), similar to the majority of our directly measured T thus far. Comparable distributions are also found for early-type galaxies in the ATLAS^{3D} and SAMI surveys (A.-M. Weijmans et al. 2014; C. Foster et al. 2017) and for simulated massive slow rotators in the IllustrisTNG simulations (C. Pulsoni et al. 2020). We therefore expect stellar halos with the prolateness of NGC 315 to be a rare occurrence.

3.2.3. Stellar Orbital Structure

The composition of the major types of orbits in the best-fit model for NGC 315 is plotted as a function of radius in the upper panel of Figure 5. The two types of tube orbits have a fixed sense of rotation, with short- and long-axis tubes having angular momentum components along the intrinsic short- and long-axis, respectively, which do not change sign. For the box orbits, all three components of the angular momentum change sign, leaving no sense of rotation for this orbit type. The relative contribution of these three orbit types determines the velocity structure of the galaxy.

Figure 5 shows that 45%–60% of the mass in the orbits is from long-axis tubes, while short-axis tubes and box orbits contribute comparable amounts to the remaining orbital weight. The predominance of long-axis tubes over short-axis tubes reflects the prolateness of NGC 315. This is opposite to the orbital compositions in oblate triaxial galaxies with T < 0.5, e.g., about 60–70% of orbits are short-axis tubes while \sim 20% are long-axis tubes in NGC 1453 and NGC 2693 (M. E. Quenneville et al. 2021; J. D. Pilawa et al. 2022).

Further insight into the relative short- and long-axis tube orbits can be gained from the relationship between the

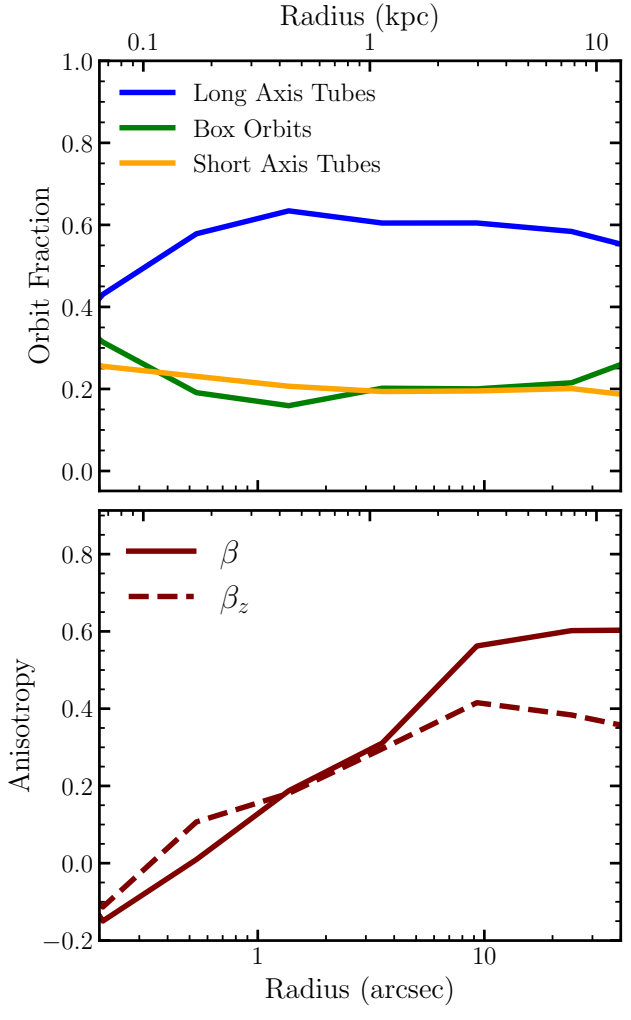


Figure 5. Composition of the three major orbit types (upper panel) and velocity anisotropy (lower panel) as a function of radius in the best-fit triaxial galaxy model of NGC 315. The majority of the orbital weights are in long-axis tube orbits, consistent with the prolateness of the galaxy. Short-axis tube orbits and box orbits both contribute about 20%–25% to the remaining orbital weights. The velocity anisotropy parameters $\beta \equiv 1 - \sigma_t^2/\sigma_r^2$ (in spherical coordinates) and $\beta_z = 1 - \sigma_z^2/\sigma_R^2$ (in cylindrical coordinates) indicate the stellar orbits are mildly tangentially anisotropic at small radii and are increasingly radially anisotropic at larger radii.

parameter T and the locations in the start space from which the tube orbits are generated (using the scheme of M. Schwarzschild 1993). M. E. Quenneville et al. (2021) shows that the location of the focal curve demarcating the regions in start space populated by long- and short-axis tubes (their Figure 1) is specified by an angle η , where $\tan \eta \approx \sqrt{T/(1-T)}$. For T=0.89, we have $\eta \approx 71^\circ$, indicating the long- and short-axis tube fraction in the start space is 79% and 21%, respectively, corresponding to a ratio of about 4–1. The actual orbital fractions for the best-fit galaxy model shown in Figure 5 are computed from these base orbits with the corresponding orbital weights, yielding a comparable long-to-short tube ratio of roughly 3–1.

The lower panel of Figure 5 displays the radial profile of the velocity anisotropy parameters, $\beta=1-\sigma_t^2/\sigma_r^2$ and $\beta_z=1-\sigma_z^2/\sigma_R^2$, where σ_t and σ_r are the tangential and radial velocity dispersions in spherical coordinates, and σ_z and σ_R are the vertical and radial velocity dispersions in cylindrical coordinates, respectively. The orbits in the central portion of NGC 315 are slightly tangential with $\beta < 0$ and become radially anisotropic away from the center. This trend is typical in massive elliptical galaxies (e.g., J. Thomas et al. 2016) and can be seen in other MASSIVE galaxies (e.g., E. R. Liepold et al. 2020; J. D. Pilawa et al. 2022).

4. Discussion

4.1. Uncertainties in Central Surface Brightness

A primary systematic uncertainty in the mass measurements of NGC 315 SMBH is the effect of dust on the observed central stellar light. In the main analysis above, we have used MGE model A of B. D. Boizelle et al. (2021) to approximate the surface brightness profile of NGC 315. To test the impact of the adopted profile on the inferred $M_{\rm BH}$, we replace it with their MGE B3, the model that assumes the largest extinction correction. We rerun orbit models and parameter search in the reduced 3D space of $M_{\rm BH}$, M^*/L , and halo mass with the shape parameters fixed to the best-fitting values. While model B3 has a significantly higher central luminosity density than model A (see Appendix), the difference is confined to the inner ~ 0.5 , a scale comparable to the PSF of our Gemini observations. It is thus not surprising that our tests find $\lesssim 3\%$ changes in the best-fitting parameters, with $M_{\rm BH}=(2.9\pm0.2)\times 10^9 M_{\odot}$ and $M^{\prime}/$ $L=2.45\pm0.04\,M_{\odot}/L_{\odot}$. In comparison, B. D. Boizelle et al. (2021) find that switching from model A to B3 in their CObased study reduces $M_{\rm BH}$ and M^*/L by $\sim 18\%$. One possible reason for this larger change in their tests is the CO kinematic data only extend to ~ 1 ", and thus their constraints are more sensitive to changes in the central luminosity density and the enclosed mass.

4.2. M_{BH} from Stellar versus CO Kinematics

With the mass measurement of NGC 315's SMBH presented in this paper, there are now seven galaxies whose SMBH masses have been determined from the kinematics of both CO and stars (with orbit-based modeling). A summary of these measurements is given in Table 2 and Figure 6. To assess the level of agreement between $M_{\rm BH}$ from the two methods, we perform a linear fit using the LinMix package (B. C. Kelly 2007). This method derives the best-fitting line through hierarchical Bayesian modeling, accounting for uncertainties in both x and y directions. It models the distribution of the independent variable as a mixture of Gaussians and assumes the dependent variable is drawn from a Gaussian distribution centered on a linear relation with the independent variable. The code returns posterior distributions for the parameters, including an intrinsic scatter term representing the variance beyond measurement uncertainties.

The resulting linear fit for $M_{\rm BH}$ from the two methods is $\log_{10}(M_{\rm BH}^{\rm CO}/10^9 M_{\odot}) = (1.15^{+0.44}_{-0.41})\log_{10}(M_{\rm BH}^{\rm stellar}/10^9 M_{\odot}) - (0.12 \pm 0.15)$, with an intrinsic scatter of $\epsilon = 0.35^{+0.26}_{-0.12}$ dex (blue lines in Figure 6). To assess whether the data prefer a one-to-one model with a fixed slope of 1 and intercept of 0 or a linear relation with free coefficients, we compare the marginal

The preferred viewing angles (in Table 1) are close to the intermediate axis $(\theta = \phi = 90^\circ)$. In this limit, the freedom for the deprojection extends roughly along the intermediate axis, corresponding to different values of T (see Equations (7) and (8) of M. E. Quenneville et al. 2022). Within the viewing-angle parameterization of the deprojection, the third viewing-angle ψ then sets T.

 Table 2

 Galaxies with Dynamical $M_{\rm BH}$ Measurements from Both Stellar and CO Kinematics

	Stellar-based Measurements			CO-based Measurements				
Name	D (Mpc)	$M_{ m BH}$ (10^9M_{\odot})	M^*/L [band]	i	$M_{\rm BH} \ (10^9 M_{\odot})$	M^*/L [band]	i	References
(1)	(2)	(3)	(4)	(5)	(6)	(7)	(8)	(9)
NGC 315	65.9	3.0 ± 0.2	$2.49 \pm 0.06 [J]$	N/A (triaxial)	$1.96^{+0.30}_{-0.13}$	$1.86 \pm 0.01 \ [J]$	$74^{\circ}.1 \pm 0^{\circ}.1$	(a, b)
NGC 524 ^a	23.3	$0.83^{+0.09}_{-0.04}$	$5.8 \pm 0.4 \ [I]$	20° (fixed)	$0.40^{+0.12}_{-0.07}$	$5.7 \pm 0.3 \ [I]$	20° (fixed)	(c, d)
NGC 1332	22.3	1.45 ± 0.2	$7.08 \pm 0.39 \ [R]$	90° (fixed)	$0.664^{+0.065}_{-0.063}$	7.83 [R]	85 [°] .2	(e, f)
NGC 3258	31.9	2.2 ± 0.2	$2.5 \pm 0.1 \ [H]$	48° (fixed)	2.249 ± 0.27	$\cdots [H]$	27.5-49.3	(g, h)
NGC 4697	11.4	0.18 ± 0.05	$4.3 \pm 0.3 \ [V]$	90° (fixed)	$0.13^{+0.003}_{-0.006}$	$2.14^{+0.04}_{-0.05}$ [i]	$76.1^{\circ +0.5\circ}_{00000000000000000000000000000000000$	(i, j)
NGC 4751	26.9	1.4 ± 0.1	$12.2^{+0.6}_{-0.7}$ [R]	90° (fixed)	$3.43^{+0.16}_{-0.16}$	$2.68 \pm 0.11 \ [H]$	$78.7^{\circ +0.1}_{00000000000000000000000000000000000$	(k, l)
NGC 6861	27.3	2.0 ± 0.2	$6.1^{+0.2}_{-0.1}$ [I]	90° (fixed)	1–3	2.14-2.52 [H]	72.7–73.6	(k, m)

Notes. Column (1): Galaxy name. Column (2): Distance. Different values are assumed in the CO versus stellar studies for NGC 315 (this paper) and NGC 4697; the surface brightness fluctuation distance is adopted here and all measurements are scaled to this value. Column (3): Black hole mass from stellar-based measurements. Column (4): Stellar mass-to-light ratio for the stellar-based measurements (band indicated in square brackets). Column (5): Inclination angle assumed in axisymmetric orbit modeling; only NGC 315 is modeled with a triaxial orbit code. Column (6): Black hole mass from CO-based measurements. Column (7): Stellar mass-to-light ratio for the CO-based measurements (band indicated in square brackets). Column (8): Inclination from CO-based measurements. Column (9): References. (a) This work, (b) B. D. Boizelle et al. (2021), (c) D. Krajnovic et al. (2009), (d) M. D. Smith et al. (2019), (e) S. P. Rusli et al. (2011), (f) A. J. Barth et al. (2016), (g) T. K. Waters et al. (2024), (h) B. D. Boizelle et al. (2019), (i) A. Schulze & K. Gebhardt (2011), (j) T. A. Davis et al. (2017), (k) S. P. Rusli et al. (2013), (l) P. Dominiak et al. (2024), (m) K. M. Kabasares et al. (2022).

^a The reported errors for NGC 524 parameters are 3σ regions; we divide them by 3 to approximate the 1σ regions, as quoted for all other galaxies.

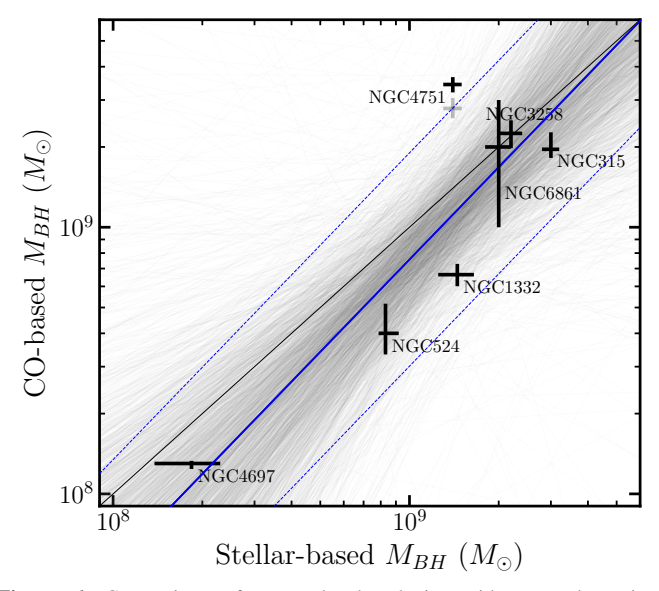


Figure 6. Comparison of seven local galaxies with $M_{\rm BH}$ determined independently from stellar and CO kinematics listed in Table 2. The median linear fit (solid blue line) is given by $\log_{10}(M_{\rm BH}^{\rm CO}/10^9 M_{\odot}) = (1.15^{+0.44}_{-0.41})\log_{10}(M_{\rm BH}^{\rm stellar}/10^9 M_{\odot}) - (0.12 \pm 0.15)$, with an intrinsic scatter of $\epsilon = 0.35^{+0.26}_{-0.12}$ dex (dotted blue lines). Faint gray lines are constructed from sampling over the posteriors for our parameters. The solid black line denotes the one-to-one line to guide the eye. The two points for NGC 4751 represent $M_{\rm BH}$ inferred when assuming a spatially varying (lower point) vs. constant (upper point) M^{*}/L in the CO-based model (see text).

evidence ratio ("Bayes factor") of the two models. The one-to-one model here is a subset of the free linear model, so the Bayes factor in this case quantifies the factor by which a free slope and intercept improves the fit. Using dynesty, we find a log-marginal evidence difference of $\Delta \ln Z = 2.78 \pm 0.02$ (one-to-one model minus free model), which is much less than what is typically considered evidence in favor of one model (e.g., $|\Delta \ln Z| > 5$, R. Trotta 2008; W. Lockhart & S. E. Gralla 2022). We therefore conclude that while there are differences in individual $M_{\rm BH}$ values determined from CO and stellar

kinematics, there is no evidence for statistically significant biases between the two methods in the current data.

5. Summary

We have performed triaxial stellar-orbit modeling of the massive elliptical galaxy NGC 315 using photometric data and \sim 2300 spatially resolved stellar kinematic measurements in 304 bins covering a radial range of \sim 0."3–30" from the MASSIVE survey as constraints. After searching over \sim 15,000 galaxy models with an efficient Bayesian scheme, we are able to simultaneously constrain NGC 315's $M_{\rm BH}$, M^*/L , dark matter halo mass, and intrinsic shape parameters.

We find NGC 315 to be a triaxial and highly prolate galaxy with a triaxiality parameter $T=0.89\pm0.02$, hosting an SMBH with $M_{\rm BH}=(3.0\pm0.3)\times10^9 M_{\odot}$. At this dynamically inferred mass, the NGC 315 SMBH is located below the mean $M_{\rm BH}-\sigma$ and $M_{\rm BH}-M_{\rm bulge}$ scaling relations formed by other local SMBHs and their host galaxies, but it lies within the intrinsic scatter of these relations. In comparison, the SMBH mass inferred from CO kinematics is $M_{\rm BH}=(1.96^{+0.30}_{-0.13})\times10^9 M_{\odot}$ (scaled to our distance).

The orbit-based $M_{\rm BH}$ determination reported in this paper adds a measurement to a small but growing sample of galaxies for which the mass of the central SMBH has been measured using more than one dynamical tracer. Comparing $M_{\rm BH}$ values for a sample of seven galaxies with both CO-based and stellar-orbit-based measurements, we find that the one-to-one relation with an intrinsic scatter term has roughly the same support as a linear relation with free slope, intercept, and intrinsic scatter. The current data therefore do not indicate statistically significant biases between the masses inferred from the two methods.

At our best estimates of $M_{\rm BH}=3.0\times10^9 M_{\odot}$ and $D=65.9\,{\rm Mpc}$, the NGC 315 SMBH has an angular shadow size of $\theta=2\sqrt{27}\,GM_{\rm BH}/c^2D\approx4.7\,\mu{\rm as}$. Together with its relatively high millimeter flux, NGC 315 is a prime candidate target for future event horizon scale imaging missions (e.g., Y. Ben Zineb et al. 2024; M. D. Johnson et al. 2024;

X. A. Zhang et al. 2025). A successful measurement of the shadow size would provide another independent estimate of this SMBH's mass.

Acknowledgments

We acknowledge support from NSF-AST-2206219, NSF-AST-2206307, and the Heising-Simons Foundation. This work used the Extreme Science and Engineering Discovery Environment (XSEDE) at the San Diego Supercomputing Center through allocation AST180041, which is supported by NSF grant ACI-1548562. Portions of this research were conducted with the advanced computing resources provided by Texas A&M High Performance Research Computing. This work is based in part on data obtained at the international Gemini Observatory, a program of NSF's NOIRLab, which is managed by the Association of Universities for Research in Astronomy (AURA) under a cooperative agreement with the National Science Foundation on behalf of the Gemini partnership: the National Science Foundation (United States), the National Research Council (Canada), Agencia Nacional de Investigación y Desarrollo (Chile), Ministerio de Ciencia, Tecnología e Innovación (Argentina), Ministério da Ciência, Tecnologia, Inovações e Comunicações (Brazil), and Korea Astronomy and Space Science Institute (Republic of Korea). This work is based in part on observations made with the NASA/ESA Hubble Space Telescope, obtained at the Space Telescope Science Institute, which is operated by the Association of Universities for Research in Astronomy, Inc., under NASA contract NAS5-26555. These observations are associated with program GO-14219.

Software: Astropy (Astropy Collaboration et al. 2013, 2018), Dynesty (J. S. Speagle 2020), Galfit (C. Y. Peng et al. 2002), jampy (M. Cappellari 2008), linmix (B. C. Kelly 2007), Matplotlib (J. D. Hunter 2007), mgefit (M. Cappellari 2002), NumPy (C. R. Harris et al. 2020).

Appendix

We include a comparison of the deprojected 3D luminosity density for the three MGE models described in the text in Figure 7.

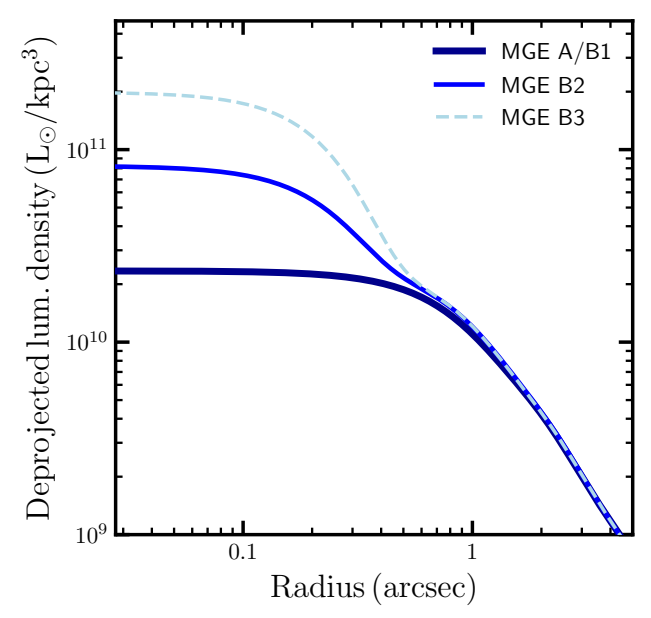


Figure 7. Comparison of the deprojected 3D luminosity density for the three MGE models of NGC 315 presented in B. D. Boizelle et al. (2021). The large bumps in the central 3D luminosity densities of model B2 and B3 are artifacts of the small widths of the central Gaussian component of these two models, $\sigma' = 0''178$ and 0''119, respectively. In comparison, model A has $\sigma' = 0''580$ for the central component and is well behaved upon deprojection.

ORCID iDs

Jacob Pilawa https://orcid.org/0000-0001-7040-9117
Emily R. Liepold https://orcid.org/0000-0002-7703-7077
Chung-Pei Ma https://orcid.org/0000-0002-4430-102X
Jonelle L. Walsh https://orcid.org/0000-0002-1881-5908
Jenny E. Greene https://orcid.org/0000-0002-5612-3427

References

Astropy Collaboration, Price-Whelan, A. M., Sipöcz, B. M., et al. 2018, AJ, 156, 123

Astropy Collaboration, Robitaille, T. P., Tollerud, E. J., et al. 2013, A&A, 558, A33

Barth, A. J., Boizelle, B. D., Darling, J., et al. 2016, ApJL, 822, L28
Barth, A. J., Ho, L. C., & Sargent, W. L. W. 2002, AJ, 124, 2607
Ben Zineb, Y., Ozel, F., & Psaltis, D. 2024, arXiv:2412.01904
Blakeslee, J. P., Jensen, J. B., Ma, C.-P., Milne, P. A., & Greene, J. E. 2021, ApJ, 911, 65

```
Boizelle, B. D., Barth, A. J., Walsh, J. L., et al. 2019, ApJ, 881, 10
Boizelle, B. D., Walsh, J. L., Barth, A. J., et al. 2021, ApJ, 908, 19
Cappellari, M. 2002, MNRAS, 333, 400
Cappellari, M. 2008, MNRAS, 390, 71
Cappellari, M. 2017, MNRAS, 466, 798
Cappellari, M., Scott, N., Alatalo, K., et al. 2013, MNRAS, 432, 1709
Cenarro, A. J., Cardiel, N., Gorgas, J., et al. 2001, MNRAS, 326, 959
Crook, A. C., Huchra, J. P., Martimbeau, N., et al. 2007, ApJ, 655, 790
Davidson, J. R., Boizelle, B. D., Walsh, J. L., et al. 2024, ApJ, 972, 127
Davis, T. A., Bureau, M., Onishi, K., et al. 2017, MNRAS, 468, 4675
Dominiak, P., Cappellari, M., Bureau, M., et al. 2024, arXiv:2404.11260
Ene, I., Ma, C.-P., McConnell, N. J., et al. 2019, ApJ, 878, 57
Ene, I., Ma, C.-P., Veale, M., et al. 2018, MNRAS, 479, 2810
Ene, I., Ma, C.-P., Walsh, J. L., et al. 2020, ApJ, 891, 65
Falcón-Barroso, J., Sánchez-Blázquez, P., Vazdekis, A., et al. 2011, A&A,
   532, A95
Fanaroff, B. L., & Riley, J. M. 1974, MNRAS, 167, 31P
Foster, C., Van De Sande, J., D'Eugenio, F., et al. 2017, MNRAS, 472, 966
Goulding, A. D., Greene, J. E., Ma, C.-P., et al. 2016, ApJ, 826, 167
Goullaud, C. F., Jensen, J. B., Blakeslee, J. P., et al. 2018, ApJ, 856, 11
Harris, C. R., Millman, K. J., van der Walt, S. J., et al. 2020, Natur, 585, 357
Hunter, J. D. 2007, CSE, 9, 90
Jensen, J. B., Blakeslee, J. P., Ma, C.-P., et al. 2021, ApJS, 255, 21
Johnson, M. D., Akiyama, K., Baturin, R., et al. 2024, Proc. SPIE, 13092, 821
Kabasares, K. M., Barth, A. J., Buote, D. A., et al. 2022, ApJ, 934, 162
Kelly, B. C. 2007, ApJ, 665, 1489
Krajnovic, D., McDermid, R. M., Cappellari, M., & Davies, R. L. 2009,
   MNRAS, 399, 1839
Laing, R. A., Canvin, J. R., Cotton, W. D., & Bridle, A. H. 2006, MNRAS,
  368. 48
Lawson, C. L., & Hanson, R. J. 1995, Solving Least Squares Problems
   (Philadelphia, PA: SIAM)
Liepold, E. R., & Ma, C.-P. 2024, ApJL, 971, L29
Liepold, E. R., Ma, C.-P., & Walsh, J. L. 2023, ApJL, 945, L35
Liepold, E. R., Ma, C.-P., & Walsh, J. L. 2025, ApJ, 980, 58
Liepold, E. R., Quenneville, M. E., Ma, C.-P., et al. 2020, ApJ, 891, 4
Lipka, M., & Thomas, J. 2021, MNRAS, 504, 4599
```

Lockhart, W., & Gralla, S. E. 2022, MNRAS, 517, 2462

Ma, C.-P., Greene, J. E., McConnell, N., et al. 2014, ApJ, 795, 158

```
Magorrian, J. 2006, MNRAS, 373, 425
McConnell, N. J., & Ma, C.-P. 2013, ApJ, 764, 184
McKay, M. D., Beckman, R. J., & Conover, W. J. 1979, Technometrics: A
   Journal of Statistics for the Physical, Chemical, and Engineering Sciences,
  21, 239, http://www.jstor.org/stable/1268522
Navarro, J. F., Frenk, C. S., & White, S. D. M. 1996, ApJ, 462, 563
Peng, C. Y., Ho, L. C., Impey, C. D., & Rix, H.-W. 2002, AJ, 124, 266
Pilawa, J., Liepold, E. R., & Ma, C.-P. 2024, ApJ, 966, 205
Pilawa, J. D., Liepold, E. R., Delgado Andrade, S. C., et al. 2022, ApJ,
  928, 178
Pulsoni, C., Gerhard, O., Arnaboldi, M., et al. 2020, A&A, 641, A60
Quenneville, M. E., Blakeslee, J. P., Ma, C.-P., et al. 2024, MNRAS,
   527, 249
Quenneville, M. E., Liepold, E. R., & Ma, C.-P. 2021, ApJS, 254, 25
Quenneville, M. E., Liepold, E. R., & Ma, C.-P. 2022, ApJ, 926, 30
Ricci, L., Boccardi, B., Nokhrina, E., et al. 2022, A&A, 664, A166
Rusli, S. P., Thomas, J., Erwin, P., et al. 2011, MNRAS, 410, 1223
Rusli, S. P., Thomas, J., Saglia, R. P., et al. 2013, AJ, 146, 45
Saglia, R. P., Opitsch, M., Erwin, P., et al. 2016, ApJ, 818, 1579
Sanchez-Blazquez, P., Peletier, R. F., Jimenez-Vicente, J., et al. 2006,
   MNRAS, 371, 703
Santucci, G., Brough, S., Van De Sande, J., et al. 2022, ApJ, 930, 153
Schulze, A., & Gebhardt, K. 2011, ApJ, 729, 21
Schwarzschild, M. 1993, ApJ, 409, 563
Smith, M. D., Bureau, M., Davis, T. A., et al. 2019, MNRAS, 485, 4359
Speagle, J. S. 2020, MNRAS, 493, 3132
Thomas, J., Ma, C.-P., McConnell, N. J., et al. 2016, Natur, 532, 340
Trotta, R. 2008, ConPh, 49, 71
Van Den Bosch, R. C. E., Van De Ven, G., Verolme, E. K., Cappellari, M., &
  De Zeeuw, P. T. 2008, MNRAS, 385, 647
Veale, M., Ma, C.-P., Greene, J. E., et al. 2017a, MNRAS, 471, 1428
Veale, M., Ma, C.-P., Greene, J. E., et al. 2018, MNRAS, 473, 5446
Veale, M., Ma, C.-P., Thomas, J., et al. 2017b, MNRAS, 464, 356
Waters, T. K., Gültekin, K., Gebhardt, K., Nagar, N., & Ávila, V. 2024, ApJ,
  971, 149
Weijmans, A.-M., De Zeeuw, P. T., Emsellem, E., et al. 2014, MNRAS,
  444, 3340
Ye, J. 1998, JASA, 93, 120
Zhang, X. A., Ricarte, A., Pesce, D. W., et al. 2025, ApJ, 985, 41
```